Acta Materialia 277 (2024) 120200

Contents lists available at ScienceDirect

Acta Materialia

journal homepage: www.elsevier.com/locate/actamat

Full length article

Neural network interatomic potentials for open surface nano-mechanics applications

Amirhossein D. Naghdi [a,b,*], Franco Pellegrini [c], Emine Küçükbenli [d,e], Dario Massa [a,b], F. Javier Dominguez–Gutierrez [a], Efthimios Kaxiras [e,f], Stefanos Papanikolaou [a]

[a] NOMATEN Centre of Excellence, National Center for Nuclear Research, ul. A. Sołtana 7, 05-400 Swierk/Otwock, Poland
[b] IDEAS NCBR, ul. Chmielna 69, 00-801, Warsaw, Poland
[c] International School for Advanced Studies (SISSA), Via Bonomea, 265, I-34136 Trieste, Italy
[d] Nvidia Corporation, Santa Clara, CA, USA
[e] John A. Paulson School of Engineering and Applied Sciences, Harvard University, Cambridge, MA 02138, USA
[f] Department of Physics, Harvard University, Cambridge, MA 02138, USA

ARTICLE INFO

Keywords:
Neural network interatomic potentials
Nano-indentation
Nano-mechanics

ABSTRACT

Material characterization in nano-mechanical tests may provide information on the potential heterogeneity of mechanical properties. Here, we develop a robust neural-network interatomic potential (NNIP), and we provide a test for the example of molecular dynamics (MD) nanoindentation, and the case of body-centered cubic crystalline molybdenum (Mo). We employ a similarity measurement protocol, using standard local environment descriptors, to select ab initio configurations for the training dataset that capture the behavior of the indented sample. We find that it is critical to include generalized stacking fault (GSF) configurations, featuring a dumbbell self-interstitial on the surface, to capture dislocation cores, and also high-temperature configurations with frozen atom layers for the indenter tip contact. We develop a NNIP with distinct dislocation nucleation mechanisms, realistic generalized stacking fault energy (GSFE) curves, and an informative energy landscape for the atoms on the sample surface during nanoindentation. We compare our NNIP results with nanoindentation simulations, performed with three existing potentials – an embedded atom method (EAM) potential, a gaussian approximation potential (GAP), and a tabulated GAP (tabGAP) potential – that predict different dislocation nucleation mechanisms, and display the absence of essential information on the shear stress at the sample surface in the elastic region. Finally, we compared our NNIP nanoindentation results with experiments, showing reliable predictions for reduced Young's modulus and observable slip traces.

1. Introduction

Nano-mechanical tests serve as essential tools for probing the mechanical properties of materials at the nanoscale. Techniques such as nano-tensile/compression [1–3], nanoindentation [4–11], and creep testing [12] play a pivotal role in revealing the intrinsic properties of materials. This understanding, in turn, facilitates the design and production of innovative materials capable of functioning in extreme environments. These tests involve subjecting the material to controlled strain/stress at the nanoscale, enabling researchers to gain valuable insights into its mechanical response. This knowledge is crucial in the field of defect physics, as nano-mechanical tests provide a means to investigate the mechanisms of defects nucleation and their impact on the mechanical performance of materials under extreme conditions. In this study, we aim to present a comprehensive method for simulating nano-mechanical tests, taking nanoindentation as an example, on crystalline materials using neural-network interatomic potentials (NNIPs).

Nano-mechanical test techniques find application in several areas of materials science. Specifically, in situ techniques [13,14] contribute significantly to the understanding of material deformation under controlled applied stress or strain, while the specimen is simultaneously observed/measured by electron microscopic devices. These methodologies play a pivotal role in exploring materials properties at the nano scale, offering insights into the intrinsic properties of materials, such as the strength of each crystalline grain. Furthermore, these techniques prove invaluable in investigating temperature-related deformation mechanisms inherent in crystalline materials. The focus of this paper is on nanoindentation testing, a widely utilized method for

* Corresponding author at: NOMATEN Centre of Excellence, National Center for Nuclear Research, ul. A. Sołtana 7, 05-400 Swierk/Otwock, Poland.
E-mail address: Amirhossein.Naghdi@ncbj.gov.pl (A.D. Naghdi).

https://doi.org/10.1016/j.actamat.2024.120200
Received 23 April 2024; Received in revised form 14 July 2024; Accepted 14 July 2024
Available online 24 July 2024

assessing material properties on open surfaces. This technique yields results for various properties, encompassing hardness, strength, dislocation nucleation mechanisms, dislocation density, grain boundary effects, and dislocation junction formations [15–24]. However, it is essential to note that nanoindentation testing involves intricate defect nucleation mechanisms and plastic deformations, rendering accurate modeling a formidable challenge within the realm of computational materials science.

Various computational methods, such as finite element methods (FEM) [25–27], discrete dislocation dynamics (DDD) [28–32], and molecular dynamics (MD) [33–37], are employed for modeling nano-mechanical testing. In FEM, numerical solutions to differential equations in mathematical models are used to approximate and analyze the complex behavior of materials. While FEM and DDD methods prove useful in specific scenarios, they lack atomic-level precision, thereby falling short of achieving the desired level of accuracy. On the other hand, MD simulations can provide atomic-level insights into the dislocation dynamics of materials, given the use of interatomic potentials finely tuned for nano-mechanics in the simulations.

Machine-learned force fields (MLFFs) [38–47] offer a reliable method for modeling nano-mechanical tests with high precision. Various MLFF types, such as Gaussian Approximation Potentials (GAP) [39] and its tabulated version (tabGAP) [48], as well as active learning methods [49,50], are available in the literature. In addition, NNIPs exhibit exceptional accuracy in predicting atomic energies and forces [42,51–56], overcoming the time and system size limitations inherent in traditional ab initio molecular dynamics (AIMD) simulations. Given the ability of NNIPs to learn complex functions, such as the energy landscape of an extended dislocation in a metallic crystal, they prove to be excellent tools for modeling nano-mechanical testing simulations. MLFFs have been successfully applied to various problems, including catalysis [57,58], point defects modeling [59,60], multi-component materials modeling [61,62], and multi-phase systems [45], demonstrating their versatility. However, the exploration of nano-mechanical testing simulations using MLFFs is an area that remains to be fully explored.

In this paper, we present a study focused on the development of a robust NNIP by enhancing a starting dataset sourced from the literature [63] within the PANNA (Properties from Artificial Neural Network Architectures) framework [64]. While more complex models, such as MACE [55], offer improved accuracy, we chose PANNA to strike a balance between accuracy and simulation performance. We compare the Behler–Parrinello (BP) descriptor vectors [38] of the training dataset with those of a single crystal BCC Molybdenum configuration, indented with an embedded atom model (EAM) potential [65], to determine how closely the training dataset resembles the indentation process. This method is inspired by studies, such as those referenced in [66,67] , which utilize similarity measurements in the development of MLFFs. To improve the accuracy of the potential, we introduce high temperature configurations with a frozen layer and generalized stacking fault (GSF) configurations with a self-interstitial on the gamma surface. These configurations are designed to closely mimic atoms in the dislocation cores, on the surface, and under the indenter tip. Our results show that including these configurations in the training dataset reduces the distance between the atoms the potential is trained on and the indented sample. Finally, we present the results of an MD nanoindentation simulation using the potential trained with the modified dataset.

2. Methods

2.1. Descriptor parameters

In this work, PANNA: Properties from Artificial Neural Network Architectures [64], which utilizes Tensorflow [68] to train/evaluate fully-connected feed-forward NNIPs, is used to develop the interatomic potential, with the modified version of Behler–Parrinello (mBP) descriptors [38,69]. The mBP representation generates a fixed-size vector (the G-vector) for each atom in each configuration of the dataset. Each G-vector describes the environment of the corresponding atom of the configuration to which it belongs, up to a cutoff radius R_c. Although higher dimensional G-vectors lead to a more accurate representation of the target potential energy surface, oversized ones increase the MD simulation computational cost. In terms of the distances R_{ij} and R_{ik} of the atom i from its neighbors j and k and the angle subtended by those distances θ_{ijk}, the radial and angular G-vectors are given by:

$$G_i^{rad}[s] = \sum_{i \neq j} e^{-\eta(R_{ij}-R_s)^2} f_c(R_{ij}) \tag{1}$$

$$G_i^{ang}[s] = 2^{1-\zeta} \sum_{j,k \neq i} [1 + cos(\theta_{ijk} - \theta_s)]^{\zeta} \times e^{-\eta[\frac{1}{2}(R_{ij}+R_{ik})-R_s]^2} f_c(R_{ij}) f_c(R_{ik}) \tag{2}$$

where the smooth cutoff function (which includes the cutoff radius R_c) is given by:

$$f_c(R_{ij}) = \begin{cases} \frac{1}{2}\left[\cos\left(\frac{\pi R_{ij}}{R_c}\right) + 1\right], & R_{ij} \leq R_c \\ 0, & R_{ij} > R_c \end{cases} \tag{3}$$

and η, ζ, θ_s and R_s are parameters, different for the radial and angular parts. Table 1 shows all values selected for the descriptor parameters in this study. The choice of the cutoff value is made so that it covers up to three nearest neighbors of the center atom in the BCC Mo, which has a lattice constant of $a = 3.17$ Å, and thus the third nearest neighbor's distance is $a \times \sqrt{2} = 4.48$ Å. The length of the G-vector for a single element system is

$$|G_i[s]| = (R_s^{ang} \times \theta_s) + R_s^{rad}, \tag{4}$$

which leads to a G-vector of length 152, given the parameters reported in Table 1.

Table 1
Values of the parameters that appear in the definition of the radial and angular G-vectors, Eqs. (1), (2), (3). Where a number of components is given, the values are equispaced.

Descriptor parameter	Symbol	Value
Radial component:		
Radial exponent (Å^{-2})	η^{rad}	32
cutoff (Å)	R_c^{rad}	5
Number of R_s radial	R_s^{rad}	24
Angular component:		
Radial exponent (Å^{-2})	η^{ang}	16
cutoff (Å)	R_c^{ang}	5
Number of R_s angular	R_s^{ang}	8
Angular exponent	ζ	128
Number of θ_s	θ_s	16

2.2. Similarity measurements

In this study, a distance-based criterion, inspired by [66,67], is utilized to quantify the similarity between two distinct configurations. This criterion is subsequently extended to evaluate the closeness of two disparate datasets to one another. Consider two configurations, labeled as α and β, with n and m atoms per supercell, respectively. The distance matrix for the two configurations, $\boldsymbol{D}^{\alpha\beta}$, has a $n \times m$ dimension and each element of the matrix is the euclidean distance of atom i in α to atom j in β:

$$D_{i,j}^{\alpha\beta} = \left\| G_i^{\alpha}[s] - G_j^{\beta}[s] \right\|_2 \tag{5}$$

Where $i \in \{1, 2, \ldots, n\}$ and $j \in \{1, 2, \ldots, m\}$, and each $G[s]$ is a 152 dimensional vector, as explained in the previous section. Given this matrix, we can compute the minimum distance of each atom i in

Table 2
The original dataset from [63], showing N_s as the number of structures, N_{at} as the number of atoms per configuration, and N_{sel} as the number of selected configurations in the final dataset. The structure types in bold have been added to the original dataset.

Structure type	N_s	N_{at}	N_{sel}
Isolated atom	1	1	None
Dimer	19	2	None
Slice sample	1996	1	All
Distorted BCC	547	2	All
A15	100	8	None
C15	100	6	None
HCP	100	2	All
FCC	100	1	None
Diamond	100	2	None
Phonon	50	54	All
Self-interstitials (SIA)	32	121	14
di-Self-interstitials	14	122–252	All
Simple Cubic	100	1	None
Vacancy	210	53	All
di-Vacancy	10	118	All
tri-Vacancy	14	117	All
Liquid	45	128	None
Short range	90	53–55	None
Surface (100)	45	12	All
Surface (110)	45	12	All
Surface (111)	41	12	All
Surface (112)	45	12	All
Liquid Surface	24	128	All
γ-surface	178	12	All
GSFCs	100	18	All
GSFCs + SIA	100	55	All
Pileup	1000	32	All
HT + substrate	600	54–72	All

configuration α from any atom j in configuration β, and we define the similarity measure from α to β as the maximum among these minima, i.e.:

$$D^{\alpha\beta} = \max_i \min_j D^{\alpha\beta}_{i,j}. \tag{6}$$

It must be noted that this final quantity is not a proper distance, but a non-symmetric quantity giving us the "similarity measure" method, explained in this section, is subsequently employed to gain insights from the initial dataset. This also includes exploring ways to enhance the dataset through innovative configurations, specifically in relation to an indented supercell. For instance, one can compute the average of all $D^{\alpha\beta}$ values between atoms from two distinct datasets or configuration types within a dataset. This calculation provides an indication of the degree of (dis)similarity between considered datasets/configuration types. The same goes for measuring the similarity of a dataset to a targeted simulation, which in our case is an indented sample.

2.3. Dataset evaluation and improvement

As a starting point, we used a dataset [63] originally developed to train a MLFF within the GAP framework [39,70]. The objective was to determine whether this dataset accurately represents the atomic configurations occurring during nanoindentation simulations, for which we employed an EAM potential [65]. We then analyzed the obtained data to determine the degree of similarity between the atomic configurations in the dataset and those observed during the nanoindentation simulations.

This level of similarity is evaluated by identifying which atom j in the dataset has the minimum distance to each atom i in the indented sample. The obtained value corresponds to the *largest minimum* distance for each atom in the indented sample from all the atoms in the dataset. The concept of "distance" for two atoms i and j, refers to the l^2-norm of $G_i[s] - G_j[s]$, where $G[s]$ are the fixed-size mBP descriptor vectors [38,69], as discussed in the previous sections. To further analyze the similarity measurement method, we calculated the distances of sheared BCC configurations from a perfect BCC crystal (Fig. S10 in the supplementary material (SM)). It is shown that as the applied strain increases, the distance values also increase. This aligns with intuitive expectations, validating our similarity measurement method. To this end, we compared the configuration types present in the dataset to those of all atoms identified in the indented sample and drew conclusions based on the level of correspondence between the two sets. Through this analysis, we aimed to gain insights into the suitability of the selected dataset for studying nanoindentation behavior and identifying the underlying mechanisms governing it.

To generate a suitable dataset for training a NNIP targeted at nanoindentation simulations, it is crucial to ensure that the configurations included accurately represent the three essential regions of a sample under indentation. These regions include the atoms on the surface of the sample, which correspond to the pileup patterns, the atoms situated beneath the indenter tip that undergo significant plastic deformation, and the atoms located on the nucleated dislocation cores. The evaluation of these three critical regions and development of configurations that closely resemble them can serve as a benchmark for ML potentials for other BCC materials.

Before comparing the original dataset with the indented sample, we calculated the average minimum distance between each pair of configuration types and generated a correlation figure to visualize their proximity (Fig. 1(a)). It is evident from this figure that although the isolated atom and dimer configurations are quite distant from almost all other configurations, they are relatively close to the indented samples. However, these configurations were not included in the final dataset due to their low numbers (1 and 19, respectively), which were deemed insufficient for training a NNIP. Moreover, the A15, simple cubic (sc), diamond (dia), liquid and C15 configurations were removed from the final dataset as they were located at a distance beyond the set threshold from the indented configurations, with simple cubic, diamond, and C15 configurations having the largest distance. Furthermore, we excluded short-range configurations from the final dataset because their energies varied significantly (Fig. S1(a) in the SM), leading to training difficulties. Finally, to reduce computational cost, we kept only half of the self-interstitial configurations in the final dataset. Table 2 summarizes all modifications made to the original dataset.

Several methods can be employed to determine a "good" threshold for deciding whether to keep or remove a particular configuration from the dataset, based on its similarity to the indented configuration. In this study, we have chosen to use the start of the tail of the distribution of the minimum values in the dataset distance matrix as the threshold, which is approximately 6 based on Fig. 1(b). Fig. 1(b) also demonstrates that this value is consistent with the minimum distances between the dataset configurations and all three orientations of the indented samples. All decisions regarding whether to keep or remove a configuration from the final dataset in this study are based on this threshold.

To ensure the accuracy of the modifications made to the dataset, we removed one type of configuration from the dataset at a time and quantified the number of atoms in the indented samples that had minimum distances greater than 6 from the dataset (Fig. 1(c)). As our analysis show, the number of atoms with a minimum distance greater than 6 to the dataset does not increase when A15, diamond, Face-Centered Cubic (FCC), simple cubic, short range, isolated atom, and dimer configurations are removed, indicating the dataset's stability against the indented samples, whether these configurations are present in the dataset or not. However, upon removing Hexagonal Close-Packed (HCP) configurations, the number of atoms with a large distance from the dataset increases, which is consistent with the fact that the average minimum distance of HCP configurations to the indented samples is 5. The greatest increase in the number of atoms with a distance greater than 6 from the dataset occurs when surface configurations are removed, which underscores their importance since they represent the surface in the nanoindentation simulations.

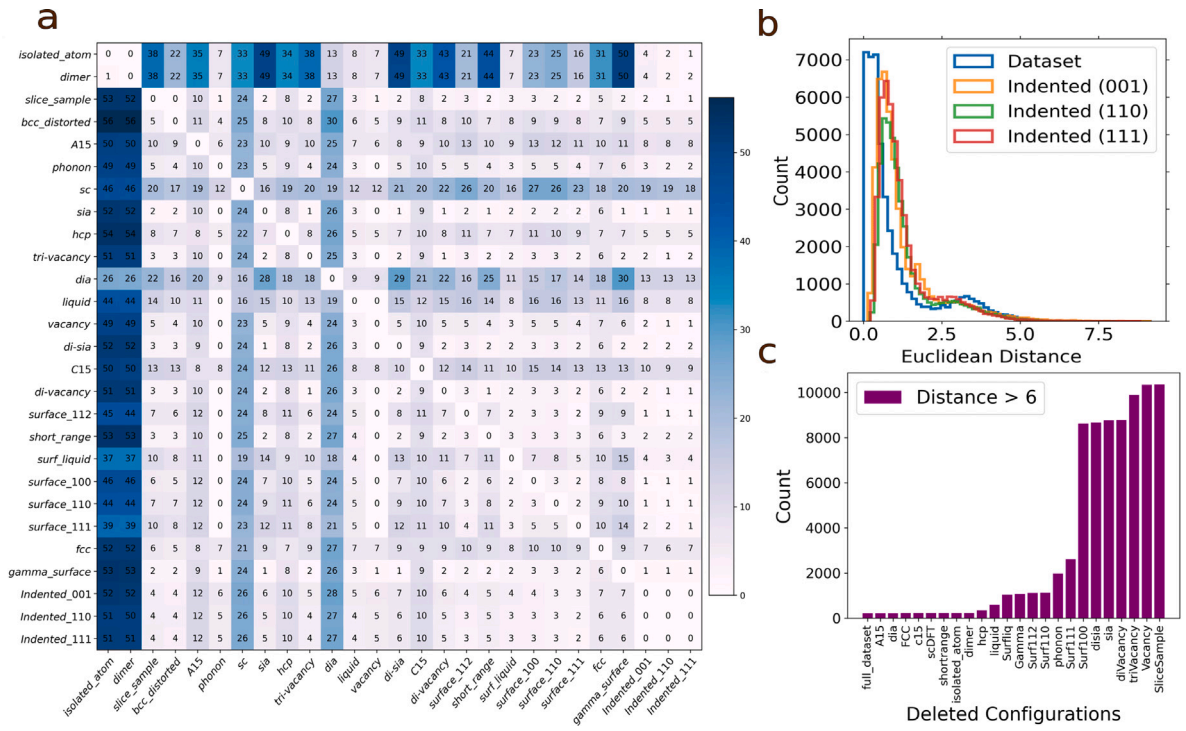

Fig. 1. Dataset evaluation and stability. (a) Average of minimum distances between different configuration types as well as with the indented samples. (b) Distribution of the minimum distances of different configurations to the rest of the data points in the dataset and the minimum distances of the dataset with the indented configurations. (c) Effect of configuration removal from the dataset on the minimum distances of the dataset to the indented sample.

Following the modifications made to the dataset obtained from [63], attempts were made to enhance its quality by incorporating various types of configurations and reevaluating the distances of the indented configuration from the dataset. Among the crucial local environments that should be included in the dataset are the atoms belonging to the dislocation cores. Furthermore, it was discovered that the distances of the atoms beneath the indenter tip and those on the surface exceeded the selected 6 threshold (Fig. 2(a)). These environments in the indented samples are critical to be covered in the dataset since dislocation cores play a vital role in the dislocation dynamics properties, and the atoms beneath the indenter tip trigger these line defects. Additionally, the plastic region beneath the surface is responsible for the pile-up patterns that appear on the surface of the indented configuration. It is also imperative to incorporate configurations in the dataset representing atoms on the surface to capture this phenomenon.

In order to model the aforementioned regions of an indented sample, we explored the use of high-temperature configurations to effectively reduce the distance between the atoms in these areas and the dataset, as depicted in Fig. 2(b). Nevertheless, accounting for the atoms beneath the indenter tip and on the surface requires the inclusion of a layer of frozen atoms in the high-temperature configurations that emulate the contact of the sample with the indenter tip. The addition of 1000 isothermal–isobaric ensemble (NPT) high-temperature configurations with 16 atoms in the $2 \times 2 \times 2$ supercells appeared to decrease the distances between the atoms on the dislocation cores and the dataset. We utilized the same approach for the atoms beneath the indenter tip. In this regard, we introduced 600 configurations, denoted as "high temperature (HT) + substrate", where a layer of atoms was frozen while other atoms were heated to high temperatures (under the melting point). While there are various unique layers of atoms that can be taken into account as the contact to the substrate, we verified that 300 configurations ($3 \times 3 \times 3$) with 54 atoms per supercell – displayed in the middle figure of Fig. 2-(b) – were adequate and most relevant after trying different layers of atoms. Additionally, we included 300 configurations ($4 \times 3 \times 3$) with 72 atoms per supercell, which featured a layer of atoms frozen on top. Moreover, it is crucial for a NNIP's dataset to incorporate configurations resembling the atoms located on the surface of the indented sample. To achieve this, we introduced 1000 BCC surface configurations ($3 \times 3 \times 2$) with 32 atoms per supercell, where a layer of atoms was frozen on top while the remaining atoms were subjected to high temperature. These configurations were named "pileup" in our study and enabled the dataset to account for the atoms in this region.

Another effective approach to cover the dislocation cores is through the use of GSFCs that incorporate a self-interstitial atom (SIA) atom on the surface (as illustrated in Fig. 3(a)). These configurations have been found to be particularly effective in reducing the distances of atoms on the dislocation cores from the dataset. While the use of GSFCs without an SIA on the surface can also reduce distances of atoms beneath the dislocation cores and on the slipping plane (as shown in Fig. 3(b)), it may not entirely cover all the atoms on the dislocation core.

Incorporating a SIA on the surface of the GSFCs leads to a significant decrease in the distances of almost all atoms on the dislocation cores from the dataset (as demonstrated in Fig. 3(c)). Notably, the use of GSFCs with a SIA instead of high-temperature configurations solely for the dislocation cores presents several advantages. For instance, the distribution of energies of these configurations is narrower, facilitating the learning process for the network (as depicted in Fig. S1((b) in the SM). Furthermore, only 100 GSFCs with SIA configurations, as opposed to the 1000 mentioned for high-temperature configurations, can ease the process of training the network. Additionally, using GSFCs with SIA configurations guarantees that no atoms on the dislocation core will have a distance greater than 6, thus ensuring the closeness of the distances of these configurations to the dislocation cores.

The visualization of the distances between the atoms in all three regions of interest and the dataset reveals a significant reduction in distances after incorporating the high-temperature configurations (see Fig. 2(c)). The distribution of distances for each region before and after adding the high-temperature configurations is depicted in Fig. 2(d). Although a few atoms still have distances greater than 6 under the

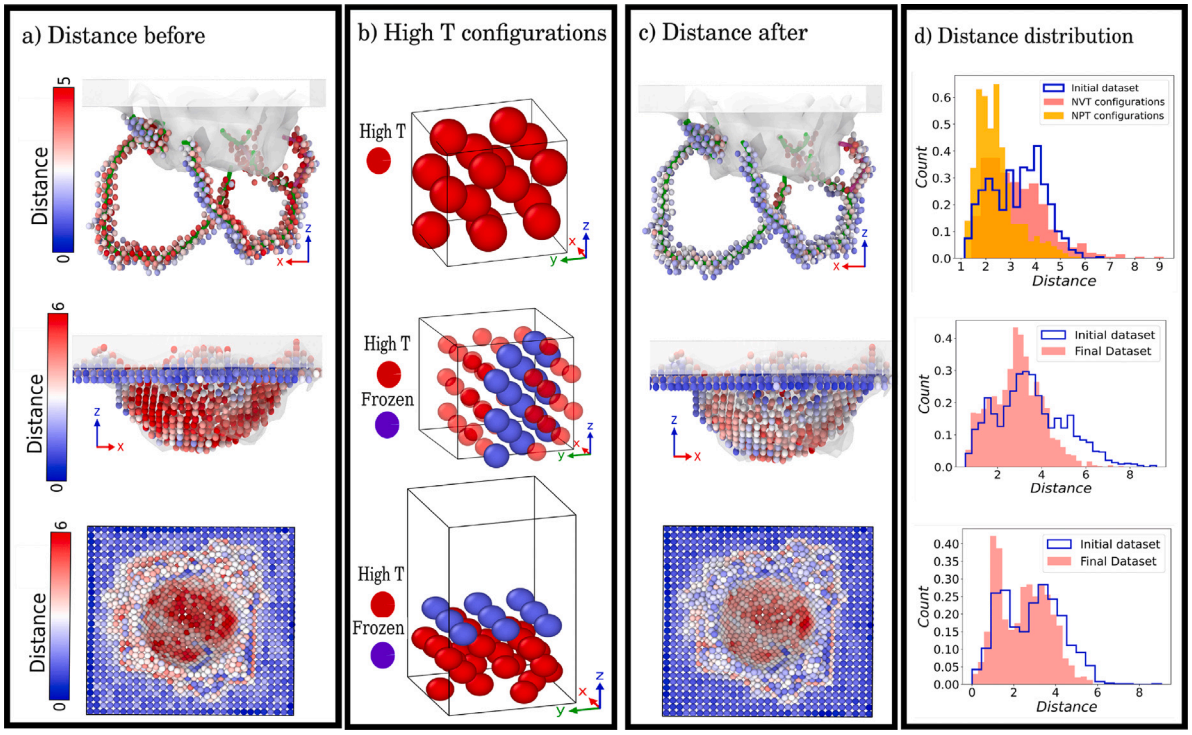

Fig. 2. Illustration of the novel configurations discovered in this study, which correspond to distinct regions of an indented sample. The figures are arranged horizontally to demonstrate the correlation between them. (a) The distances of the dislocation cores, atoms beneath the indenter tip, and pileup atoms on the surface from the original dataset. (b) The newly detected high-temperature configurations, which are associated with diverse regions of the indented sample, in terms of their distance. (c) The distance of the aforementioned regions shown in panel (a) after incorporating the newly found configurations to the dataset. (d) The distribution of distances of the aforementioned atoms from the dataset before and after incorporating the newly introduced configurations.

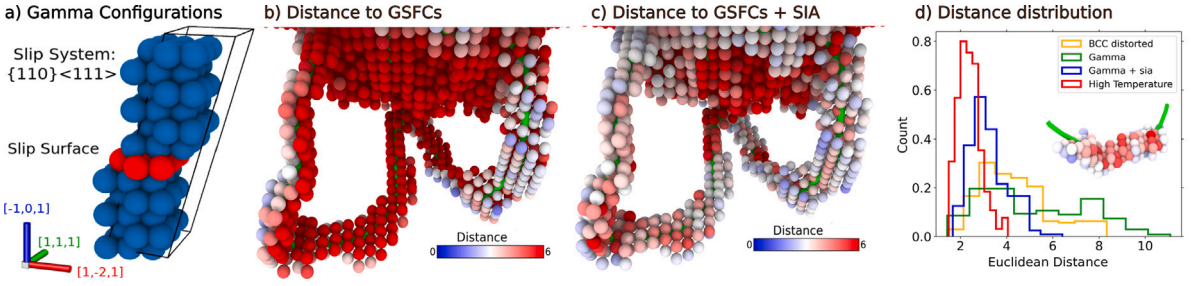

Fig. 3. The impact of incorporating GSFCs on the distances of atoms on dislocation cores from the dataset. (a) A schematic representation of the GSFCs integrated into the dataset. (b) Addition of GSFCs reduces the distances of atoms on the slip plane of dislocation cores from the dataset. (c) By including a SIA on the surface of GSFCs, all atoms on the dislocation cores can be covered. (d) The distribution of atom distances on dislocation cores reveals that GSFCs with SIA can effectively cover dislocation cores.

indenter tip, the number of such atoms has notably decreased after adding the appropriate configurations. Finally, because we are trying to develop a NNIP for the case of nanoindentation simulation during which atoms are compressed under the indenter tip, we added 300 compressed $3 \times 3 \times 4$ configurations with each of them including 72 atoms.

To further investigate the generalization of this distance-based approach, we calculated the distances of the indented samples acquired from the final trained NNIP from the final training dataset. The results are shown in Fig. S8 of the SM. The tail of the distance distributions is still lower than the threshold distance of 6 for all three regions of the indented sample. This demonstrates that the distance-based method used in this work could be expanded to mechanical simulations of at least other BCC materials.

2.4. DFT calculations

The DFT calculations were performed with the `Quantum Espresso` [71,72] (QE) package, using a norm-conserving PBEsol exchange–correlation functional [73–75] and 14 valence electrons. The Brillouin zone was sampled using Monkhorst–Pack method [76], and, from the convergence analysis of Fig. S2 in the SM, the k-point mesh and plane-wave cutoff energy in a Mo unit-cell were set to $8 \times 8 \times 8$ and 60 Ry, respectively. The selected k-point grid was rescaled for supercells calculations according to their dimension, implying the use of a $2 \times 2 \times 2$ grid for $4 \times 4 \times 4$ conventional super-cells, and was set to $1 \times 1 \times 1$ for any bigger configuration. Smearing was introduced within the Methfessel–Paxton method [77] to help convergence, with a spreading of 0.00735 Ry (0.1 eV). The structural properties, involving

elastic constants C_{ij}, Bulk modulus B (in the Voigt–Reuss–Hill approximation [78]) and Poisson ratio ν, have been computed running the QE driver `THERMO_PW` [79] on a Mo unit-cell.

The total energies of the configurations obtained from [63] were compared with the values calculated in our work to make sure of their consistency, which is shown in Fig. S4 of the SM.

2.5. Neural network training

In the PANNA framework, the environmental descriptors of each atom are provided as input to a fully connected network with two hidden layers, consisting of 256 and 128 nodes for the first and second layers, respectively, both with Gaussian activation function, and a single-node output layer with linear activation. The atomic environment is represented by a descriptor with 152 components, resulting in a network with 71808 weights and 385 biases. A batch size of 10 is utilized for training, while the model is trained using initial random weights and a constant learning rate of 10^{-4} throughout the training process. In this methodology, the energy of a configuration consisting of N atoms is defined as the sum of atomic energy contributions:

$$E = \sum_{i=1}^{N} E_i(G_i), \tag{7}$$

where E_i is the energy of atom i with a G-vector of G_i. The force on atom i which is situated at position $\vec{R}_i$ is given by:

$$\vec{F}_i = -\sum_j \sum_\mu \frac{\partial E_j}{\partial G_{j\mu}} \frac{\partial G_{j\mu}}{\partial \vec{R}_i} \tag{8}$$

with j labeling the atoms located within the cutoff distance of atom i and μ labeling the descriptor components.

To optimize the weights and bias parameters of the network, we use the Adam algorithm [80] to compute gradients of randomly selected batches of the training dataset. The loss function for optimizing the network weights, denoted collectively as W, consists of two terms, one for the energy $\mathcal{L}_E(W)$, and one for the forces, $\mathcal{L}_F(W)$:

$$\mathcal{L}(W) = \mathcal{L}_E(W) + \mathcal{L}_F(W). \tag{9}$$

The energy contribution is given by:

$$\mathcal{L}_E(W) = \sum_{s\in\text{batch}} \left[E_s^{\text{DFT}} - E_s(W)\right]^2 \tag{10}$$

where s refers to the atomic configuration, E_s^{DFT} is the total energy calculated from DFT (the target value) and $E_s(W)$ is the total energy predicted by the NNIP. The force contribution is given by:

$$\mathcal{L}_F(W) = \lambda_F \sum_{s\in\text{batch}} \sum_{i=1}^{N_s} \left|\vec{F}_{i;s}^{\text{DFT}} - \vec{F}_{i;s}(W)\right|^2 \tag{11}$$

with $\vec{F}_{i;s}^{\text{DFT}}$ the force obtained from DFT and $\vec{F}_{i;s}$ the force obtained from the NNIP, for atom i in configuration s; N_s is the total number of atoms in configuration s. The parameter λ_F adjusts the relative contribution of the force component and was set to $\lambda_F = 0.5$.

2.6. Nanoindentation simulations

2.6.1. Simulation method and parameters

To establish boundary conditions along the depth (dz) of the Mo samples, we divided them into three sections in the z direction during the initial stage: a frozen section with a width of approximately $0.02\times dz$, which ensured numerical cell stability; a thermostatic section about $0.08\times dz$ above the frozen section, which dissipated heat generated during nanoindentation; and a dynamical atoms section, where the interaction with the indenter tip modified the surface structure of the samples. Furthermore, we included a 5 nm vacuum section at the top of the sample as an open boundary [6]. We considered the indenter tip as a non-atomic repulsive imaginary (RI) rigid sphere and defined its force potential as

$$F(t) = K\left(\vec{r}(t) - R\right)^2, \tag{12}$$

where $K = 236$ eV/Å^3 (37.8 GPa) was the force constant, and $\vec{r}(t)$ was the position of the center of the tip as a function of time, with a radius $R = 3$ nm. In experiments, a Berkovich tip is used, which is spherical at the edge, matching our simulations and depth range studied [81]. We conducted molecular dynamics (MD) simulations using an NVE statistical thermodynamic ensemble and the velocity Verlet algorithm to emulate an experimental nanoindentation test. The x and y axes had periodic boundary conditions to simulate an infinite surface, while the z orientation had a fixed bottom boundary and a free top boundary in all MD simulations [20,34].

In our simulations, we chose $\vec{r}(t) = x_0\hat{x} + y_0\hat{y} + (z_0 \pm vt)\hat{z}$, where x_0 and y_0 were the center of the surface sample on the xy plane, and $z_0 = 0.5$ nm was the initial gap between the surface and the indenter tip. The tip moved with a speed of $v = 20$ m/s with a time step of $\Delta t = 1$ fs. We chose the maximum indentation depth to be 2.0 nm to avoid the influence of boundary layers in the dynamical atoms region.

2.6.2. Nanomechanical response of the material

The elastic nanocontact during loading process, P_{H}, is characterized by a Hertz fitting curve based on the sphere-flat surface contact and expressed [34,82] as:

$$P_{\text{H}} = \frac{4}{3} E_{\text{Hertz}} R^{1/2} h^{3/2}, \tag{13}$$

where R is the indenter radius, h is the indenter displacement, and E_{Hertz} is the reduced Young's modulus. Meanwhile, the contact pressure, P, is calculated by using a linear elastic contact mechanics formulation [5,34]:

$$P = 2\pi \left[24p \left(\frac{E_{\text{Y}} R}{1-\nu^2}\right)^2\right]^{1/3}, \tag{14}$$

with E_Y as the Young's modulus, p as the simulation load, R the indenter radius, and ν the Poisson's ratio; the radius of the contact area is obtained with the geometrical relationship:

$$\text{a}(h) = \left[3PR\left(1-\nu^2\right)/8E_{\text{Y}}\right]^{1/3} \tag{15}$$

which is related to the inner radius of the plastic region where the defects nucleate. These quantities provide an intrinsic measure of the surface resistance to a specific defect nucleation process [5,34], and yield to a universal linear relationship between P/E_Y and $a(h)/R_i$ given by

$$\frac{P}{E_Y} = \frac{0.844}{1-\nu^2} \frac{a(h)}{R_i}, \tag{16}$$

where $a(h)/R_i$ can be considered as the nanoindentation strain.

To determine the strength and stability of the Mo matrix under load, we compute the principal stress applied on the z direction as [9] :

$$\sigma_{zz} = -S\left[\left(1 - \frac{\arctan(\alpha)}{\alpha}\right)(1+\nu) - \frac{1}{2(1+1/\alpha^2)}\right], \tag{17}$$

where the quantities S and α are defined as:

$$S = \frac{3P_{\text{ave}}}{2\pi \text{a}(h)^2}, \quad \alpha = \frac{\text{a}(h)}{h}.$$

with h as the indentation depth and $a(h)$ the contact area between the indenter tip and the top atomic layers. The stress applied in the direction parallel to the indenter surface is then expressed as:

$$\sigma_{xx} = \sigma_{yy} = -\frac{S}{1+1/\alpha^2} \tag{18}$$

This gives the maximum shear stress:

$$\tau_{\max} = \frac{1}{2}\left(\sigma_{zz} - \sigma_{xx}\right), \tag{19}$$

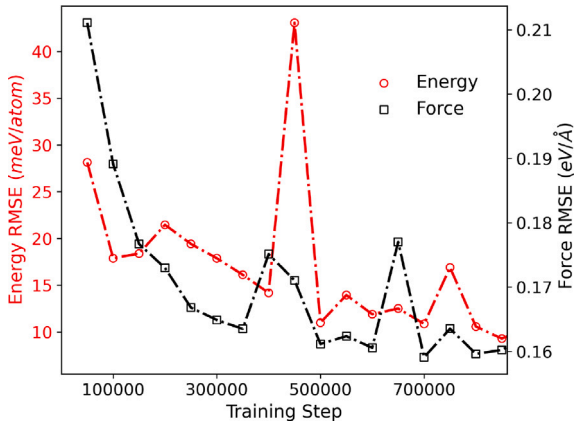

Fig. 4. Prediction of the Energies and forces for the validation set during the NNIP training.

that the material can withstand before it begins to undergo plastic deformation, being normalized by the applied pressure (equal to the applied force F divided by the contact area). The normalized depth is the distance from the surface of the material to the point at which the maximum shear stress occurs, normalized by the radius of the indenter that is used to apply the shear forces.

2.6.3. Defect analysis

In order to identify the defects in nanoindentation simulations, we apply the BCC Defect Analysis (BDA) developed by Möller and Biztek [83] which utilizes coordination number (CN), centrosymmetry parameter (CSP), and common neighbor analysis (CNA) techniques to detect typical defects found in bcc crystals. The characterization of the materials defects starts by calculating CN, CSP, and CNA values of all the atoms by considering a cutoff radius of $(1+\sqrt{2})/2a_0$ with a_0 as the lattice constant of Mo. Thus, the six next-nearest neighbors of perfect bcc atoms are into this cutoff and their CN value increases from 8 to 14. Consequently, BDA compares the CN and CSP values of each atom generating a list of non-bcc neighbors with CNA≠bcc and CN≠14 that classifies for the following typical defects: surfaces, vacancies, twin boundaries, screw dislocations, {110} planar faults, and edge dislocations.

2.6.4. Md simulation post-processing

All visualization of the simulations was performed using OVITO [84]. The surface areas for surface energy calculations were obtained using the “construct surface mesh" tool [85] in OVITO.

3. Results

3.1. NNIP validations

3.1.1. NNIP predictions for energies and forces

We assessed the accuracy of the trained NNIP by calculating the root mean square error (RMSE) for both energies per atom (E-RMSE) and forces components (F-RMSE) at each checkpoint saved during training. To ensure the reliability of the final model on unseen data, 10% of configurations of each structure type were reserved for validation prior to training. Fig. 4 shows that both the F-RMSE and E-RMSE decrease gradually as the network processes more data, reaching a plateau after 850 K training steps with minimum values of 9.2 meV/atom and 0.16 eV/Å, respectively.

The error distribution for both energies and forces are shown in the histogram plot of Fig. 5(a,b). The two islands in Fig. 5(a) are due to the energy difference between the pure and defected crystals. Also, the presence of three clusters in Fig. 5(b) is due to the large forces on the atoms in the defected configurations.

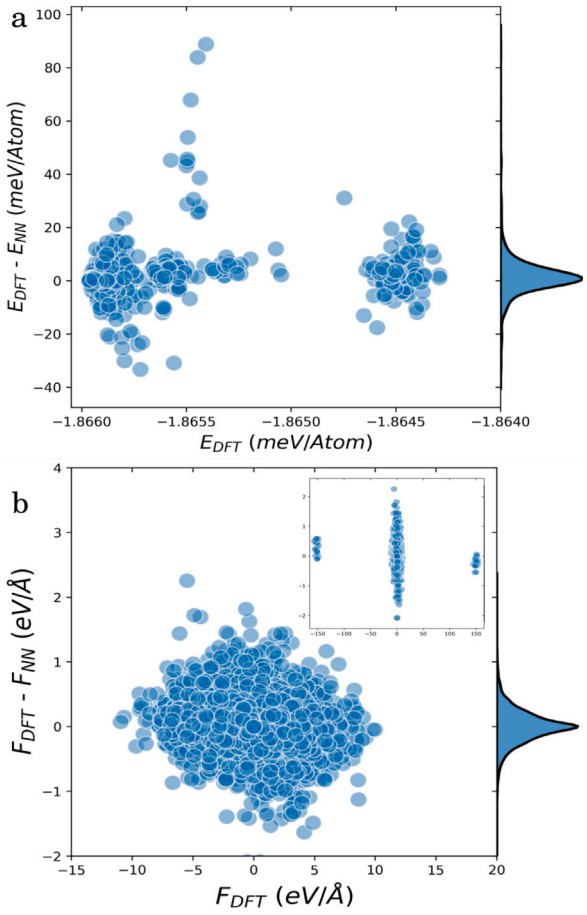

Fig. 5. NNIP error on **(a)** total energies and **(b)** forces of each atom.

3.1.2. Bulk validation

Next, we compare the elastic properties of the NNIP with both DFT and experimental results, as well as to those predicted by other interatomic potentials, such as GAP, tabGAP, and the EAM/FS potential, to evaluate the NNIP performance relative to other commonly used potentials. Table 3 summarizes the results of the comparison, explicitly reporting percentage errors with respect to the experimental values. The NNIP performs well for C_{11}, C_{44} and B, with percentage errors below 8% and in similar magnitude to GAP and EAM predictions. We here stress that the accurate prediction of the shear modulus, C_{44}, is crucial for simulating the stresses that are applied to the surface of the sample during nanoindentation, and, following the good results of EAM and GAP for this measure, the NNIP proves itself to be promising for such applications. While the largest error for the NNIP concerns the prediction of C_{12}, it can still be considered within a reasonable range as it does not exceedingly influence the prediction on B.[1]

3.1.3. NNIP accurately predicts generalized stacking fault energies (GSFE)

Finally, we compare the NNIP predictions for the GSFE against the DFT results, as well as other interatomic potentials mentioned in this work. The study focuses on the two most important slip systems of BCC crystals, namely the $\{110\}\langle\bar{1}11\rangle$ and $\{121\}\langle\bar{1}11\rangle$ families. The results were obtained for these directions in pure crystals. Additionally, since it was observed from Fig. 3 that $\{110\}\langle111\rangle$ GSF configurations with a $\langle111\rangle$ dumbbell interstitial on the surface are essential to cover the atomic environments of the dislocation core in terms of their distance

[1] We here remind that $B = \frac{1}{3}(C_{11}+2C_{12})$.

Table 3
Elastic constants C_{ij}, bulk modulus B, and Poisson ratio ν, as obtained with the GAP, tabGAP, EAM/FS and the NNIP potentials compared to DFT done in this work and experimental data. In parenthesis is reported the modulus of the percentage error with respect to the experimental value.

	GAP	tabGap	EAM	NNIP	DFT[a]	DFT[b]	Exp[c]
C_{11} (GPa)	478 (3.02%)	494 (6.47%)	465 (0.22%)	452 (2.59%)	459	468	464
C_{12} (GPa)	166 (4.40%)	146 (8.18%)	161 (1.26%)	121 (23.90%)	162	155	159
C_{44} (GPa)	108 (0.92%)	87 (20.18%)	109 (0%)	111 (1.83%)	97	100	109
B (GPa)	270 (8.00%)	262 (4.80%)	263 (5.20%)	231 (7.60%)	262	–	250
ν	0.26 (10.34%)	0.23 (20.69%)	0.26 (10.34%)	0.21 (27.59%)	0.30	–	0.29

[a] This work.
[b] Ref. [63].
[c] Ref. [86].

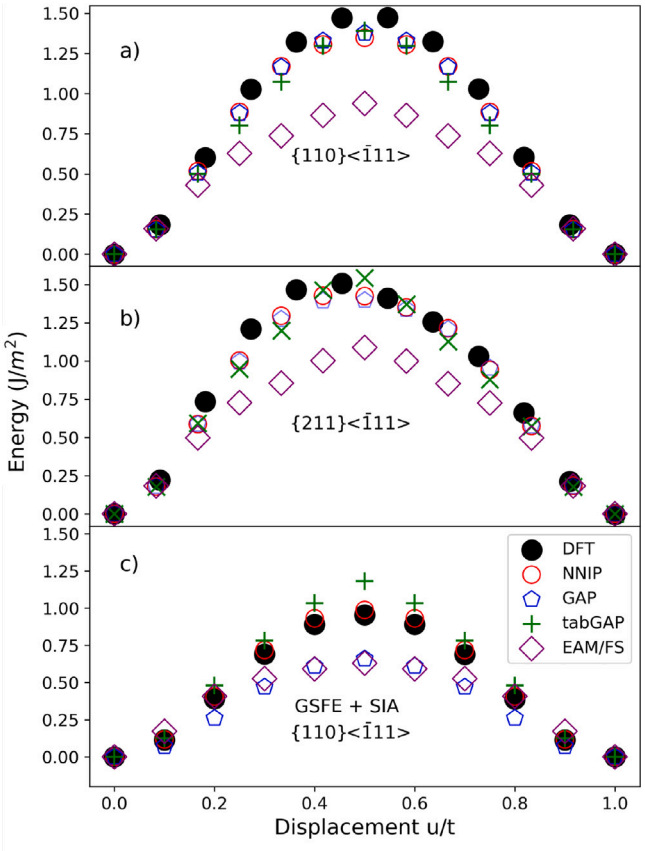

Fig. 6. Generalized Stacking Fault Energy (GSFE) for single crystalline Molybdenum for: (a) $\{110\}\langle\bar{1}11\rangle$ and (b) $\{211\}\langle\bar{1}11\rangle$. (c) The GSFE curve for the "GSFCs + SIA" configurations.

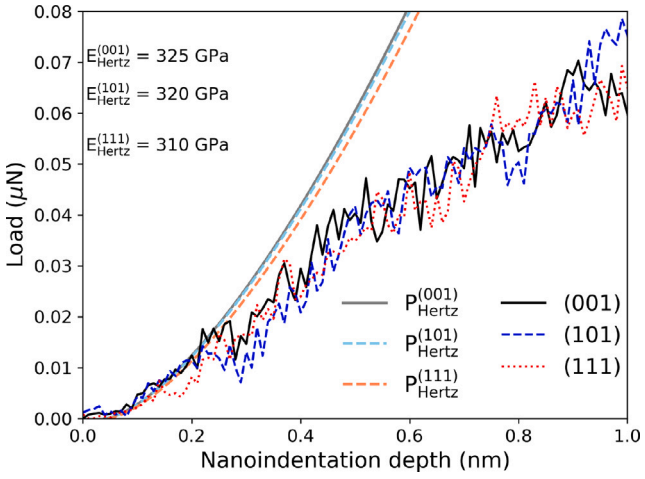

Fig. 7. Load–displacement curves for different crystal orientations, incorporating a Hertz fitting curve in the elastic region. The obtained values for the reduced Young's modulus are consistent with results from various computational approaches and experimental data [90]. Specifically, the (001), (011), and (111) crystal orientations show good agreement between experimental and simulated values, highlighting the accuracy of the developed interatomic potential, NNIP method, and ML-based atomistic approach in predicting mechanical properties.

to the indented samples, we also calculated and compared the GSFE for these configurations.

Fig. 6 shows that all potentials predict the GSFE very accurately for both slip system families and pure crystals. However, EAM/FS displays errors of about 50% and 32% for the peak of the curve for $\{110\}\langle\bar{1}11\rangle$ and $\{121\}\langle\bar{1}11\rangle$ slip families, respectively. The configurations associated with these curves are crucial, as they represent the atoms on the slip plane of an indented sample, as illustrated and discussed in Fig. 3. While it is important for an interatomic potential to accurately predict the GSFE curve for reliable dislocation modeling, it is equally crucial for the potential to correctly predict the energies and forces on the atoms for the dislocation cores. Therefore, in addition to the GSFE curves for pure crystals, we calculated the GSFE curve for configurations with a $\langle 111\rangle$ dumbbell interstitial on the surface. As depicted in Fig. 6(c), NNIP is the potential that best predicts these energies, indicating the accurate simulation of dislocation dynamics during nanoindentation. In contrast, GAP and EAM potentials showed errors of 40% and tabGAP showed an error of 20% against DFT results, indicating their inability to accurately predict these values. This is discussed further in the following section.

In Table S1 and Table S2 of the Supplementary Information, we report a comparison in the prediction of the Critical Resolved Shear (CRS) Peierls barrier and stress for the different potentials with respect to DFT level for two different Mo sample orientations. The results were obtained using the PNADIS [87] automated Peierls–Nabarro [88,89] analyzer for dislocation core structure and slip resistance. Among the inputs for the calculation are: the Poisson ratio and the Shear modulus (reportend in the Table), the burger vector and the GSFE for each potential. As it can be observed, for the $\{110\}\langle\bar{1}11\rangle$ Mo sample the NNIP provides the best energy barrier and stress predictions in comparison to DFT-accuracy. While the GAP and EAM potential underestimate in a similar way the result, tabGAP fails to capture a valuable estimate with substantial overestimates. For the $\{211\}\langle\bar{1}11\rangle$ Mo sample, similar observations can be made, with the exception of the NNIP result being close to the GAP and EAM overestimates.

3.2. Nanoindentation MD simulations

3.2.1. NNIP achieves experimentally accurate results in the hertzian regime

In Fig. 7, the load–displacement curves for the three main crystal orientations are presented, including a Hertz fitting curve in the elastic region [82]. The obtained values for the reduced Young's modulus align well with results from other computational methods and experimental data [20,90]. Specifically, for the (001) crystal orientation, the experimental value is 327 GPa, while our MD simulation with

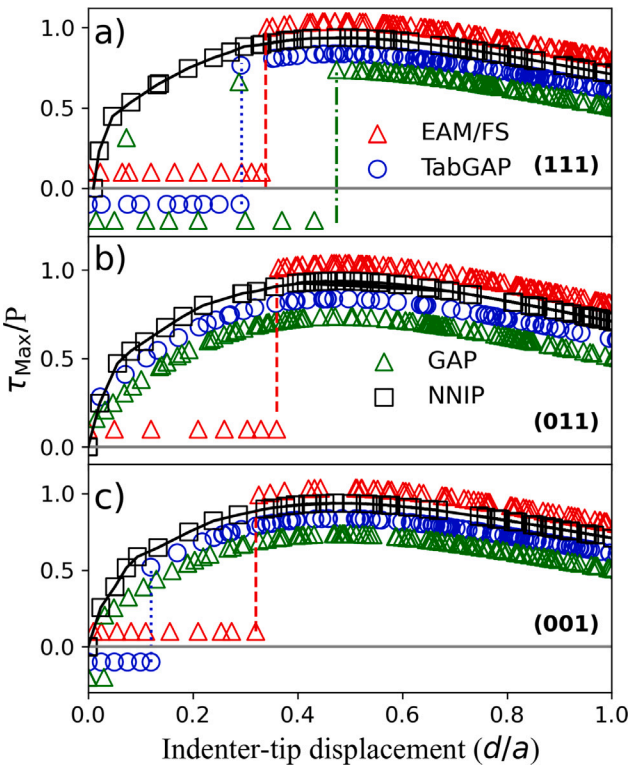

Fig. 8. Hertzian calculation of normalized maximum shear stress by the applied pressure, τ_{max}/P, as a function of normalized depth for main crystal orientations. Surface information is needed in the interatomic potentials to model nanoindentation induced plasticity in the range of 0.0 to 0.475 d/a. To aid the interpretation of the results, the values for EAM/FS were shifted by −0.1, the values for GAP were shifted by +0.2, and the values for tabGAP were shifted by +0.1 (all values in units of τ_{max}/P).

the developed NNIP yields 325 GPa. For the (011) orientation, the experimental value is 321 GPa, and NNIP method results in 320 GPa. Lastly, for the (111) orientation, the experimental value is 309 GPa, and our ML-based atomistic approach gives 310 GPa. Although these results are in excellent agreement with experimental data, the behavior of the loading curve can be obtained in a similar way by other interatomic potentials, as discussed in our previous work [34].

3.2.2. NNIP provides an informative surface energy landscape

In Fig. 8 we show results for the normalized maximum shear stress τ_{max}/P which is a dimensionless quantity, with P being the applied pressure (Eq. (14)) and τ_{max} the shear stress (Eq. (19)) calculated by using a linear elastic contact mechanics formulation [5,34], as a function of the displacement d for [001], [011], and [111] main crystal orientations [34]. A detailed explanation of the normalized shear stress calculation is provided in the Methods section. Our MD simulations report enough surface energy to model the nanoindentation induced plasticity as observed at distances close to the sample surface regardless of the crystal orientation, which is challenging for traditional and current ML interatomic potentials for BCC Mo. The modeling of the nanocontact of the indenter tip and the top atomic layers of the surface, from 0 to $\sim$ 0.3 d/a range with d the indentation depth and a the contact area, is important due to the nucleation of dislocation being dependent on this mechanisms.

The GAP simulations provide valuable insights into the interaction between the indenter tip and the top layer atoms for the (001) and (011) orientations. However, for the (111) orientation, this information is lacking, resulting in a limitation in accurately modeling the nanoindentation test before the yield point. This limitation arises due to the absence of the relevant atomic configurations in the training data for this specific potential. As a consequence, the tabGAP simulations follow a similar trend for the (111) orientation, reflecting the lack of detailed information on the interaction between the tip and the surface atoms.

In contrast, the NNIP simulations incorporate sufficient information on surface structures, allowing for a more accurate representation of the contact area. This is particularly important as the contact area depends on the applied load. The computed force between the tip and the atoms comprising the contact area is well-modeled in the NNIP simulations. The difference in spacing between data points in the elastic part of the graph is attributed to variations in the loading force, pressure, and maximum shear stress, which are considered in the contact area analysis. In addition, accurately describing the interaction between the indenter tip and the topmost atomic layers during the initial stages of nanoindentation loading is crucial for analyzing the effect of loading rate on the pop-in event. This is because the initial interaction can significantly influence the critical load required for pop-in to occur. Our NNIP simulations successfully captured the decrease in critical load with increasing loading rate (Fig. S7 in the SM), as observed experimentally [16] for different materials and in our previous work for BCC metals [34]. This suggests that NNIP effectively models the influence of the early-stage interaction on pop-in behavior. In contrast, the TabGAP simulations predicted a constant critical load regardless of loading rate, as shown in the supplementary material.

3.2.3. NNIP achieves experimentally accurate results for slip traces

In Fig. 9, we compare the results from NNIP simulations with experimental observations obtained via scanning electron microscopy (SEM) coupled with electron backscatter diffraction (EBSD) [90]. The experimental setup involved indenting a (001) Mo grain using a Berkovich tip. The computational modeling accounts for the Berkovich tip's roundness, which typically has a radius ranging from 50 to 100 nm, enabling a comparison with the early stages of nanoindentation. Upon comparing the MD simulation results obtained with different potentials to the experimental data, we find that the propagation of the slip trace along the [-110] direction closely resembles the four-folded rosette pattern observed in the MD simulation by NNIP potentials. However, notable discrepancies arise in the representation of surface information, particularly at this crystal orientation, where the NNIP simulations managed to capture the formation of pile-ups in good agreement with the experimental observations. While TabGAP and EAM potential exhibits limitations in representing the formation of pileups around the indenter tip.

From the results depicted in Fig. 8, it is evident that the interatomic potentials have limitations in representing the plastic deformation mechanisms across various crystal orientations. Specifically, for the [001] orientation, NNIP demonstrates excellent agreement with experimental data regarding surface morphology and mechanical properties. Motivated by these findings, we further investigate the surface behavior of the Mo sample at the [111] orientation, where NNIP has shown improved representation of the transition from elastic to plastic deformation compared to other potentials. In Fig. 10, we display the atomic displacement mapping of the [111] Mo sample obtained by NNIP in (a), EAM/FS in (b), GAP in (c), and tabGAP in (d) at the maximum indentation depth. The surface of the sample clearly shows displaced atoms aligned with the slip planes, forming the characteristic three-fold rosette pattern typical for BCC materials in the [111] orientation, as illustrated by the NNIP results in Fig. 10(a)). This pattern is created by $[11\bar{2}]$, $[\bar{1}01]$, and $[0\bar{1}1]$ planes [5,6]. To assist in identifying the shape of the rosette, we have added orange lines, reminiscent of what can be observed in SEM images of BCC materials [9]. Here NNIP simulations are in good agreement with typical observations of pile-up evolution. However, it is important to note that neither GAP, tabGAP, nor EAM can provide a comprehensive description due to their lack of information about open boundary simulation under external loading.

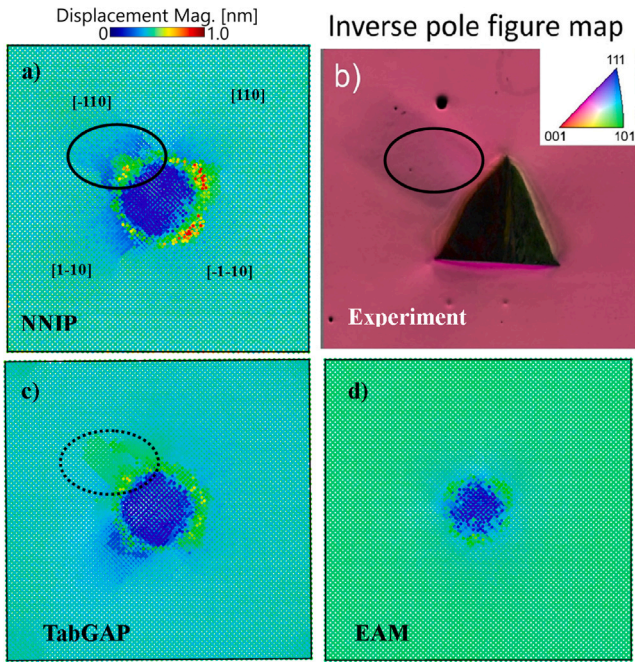

Fig. 9. Slip traces and pileup of [001] Mo at the maximum indentation depth for NNIP in (a), TabGAP in (c), and EAM in (d), compared to an experimental SEM observation reported in Ref. [90] (b). The four-fold rosette is well modeled by NNIP where the slip trace propagates on the [-110] and [1-10] planes in good qualitative agreement with the experimental result.

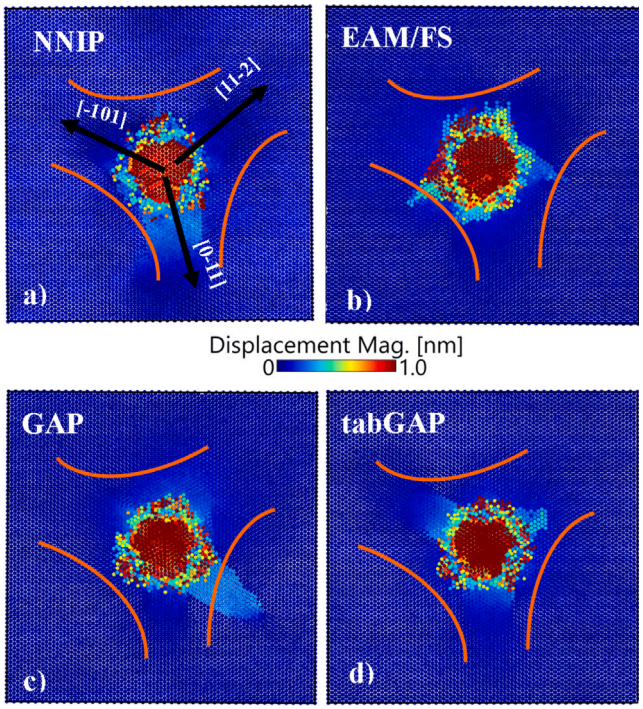

Fig. 10. Pileups and slip trace for the [111] Mo samples , at the maximum indentation depth, using different methods: NNIP in (a), EAM/FS in (b), GAP in (c), and tabGAP in (d). In this analysis, we have included an orange line to emphasize the 3-fold rosette characteristic commonly seen in the indentation of BCC samples where NNIP simulations are capable to model it [5,20,34]. (For interpretation of the references to color in this figure legend, the reader is referred to the web version of this article.)

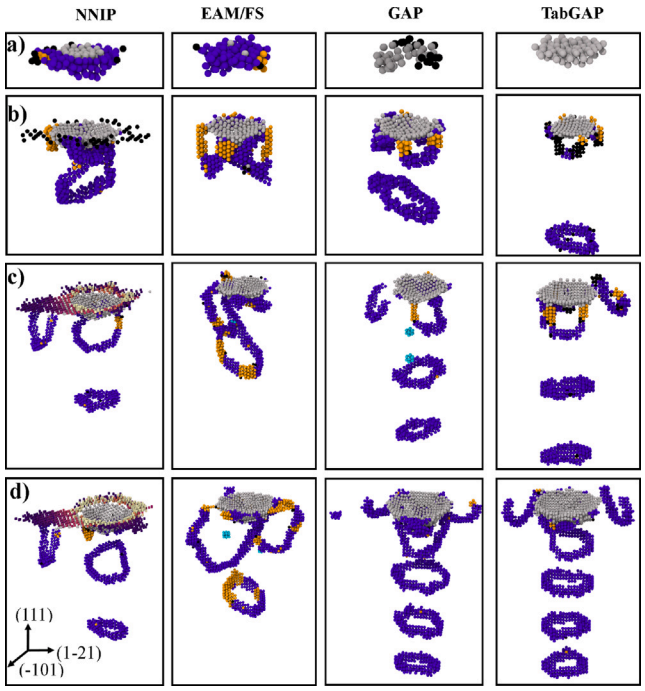

Fig. 11. Identified defects of indented (111) Mo sample by BDA method at different depths by NNIP, EAM, TabGAP, and GAP approaches. The various defect types are depicted using different colors: gray spheres represent surface atoms in direct contact with the indenter tip, blue spheres indicate edge dislocations, light-blue spheres represent atoms in the vicinity of vacancies, yellow spheres depict twin/screw dislocations, and black spheres highlight unidentified defect atoms. The nucleation and propagation of edge dislocations on the {111} slip family are observed, which then evolve into prismatic loops. In addition, identified slip traces and pile-ups are well modeled by NNIP simulations showing the well-known three-fold symmetric rosette depths below 1.45 nm that are formed by [11$\bar{2}$], [$\bar{1}$01] and [0$\bar{1}$1] planes. (For interpretation of the references to color in this figure legend, the reader is referred to the web version of this article.)

3.2.4. *NNIP demonstrates discernible dislocation nucleation stages*

Fig. 11 illustrates the defects detected using the BCC Defect Analysis (BDA) method (see Methods) in a (111) Mo sample at different depths [83]. The NNIP nanoindentation simulations in the initial stages of loading process notably enhance the description of the interaction between the indenter tip and the atoms in the uppermost layers of the surface (see Fig. 11(a)). In this context, a few Mo atoms located at the very top surface layer are recognized as surface defects. Additionally, Mo atoms situated beneath these surface defects begin to coalesce, forming edge dislocations that have the potential to evolve into shear loops, contrary to the other simulations where the interatomic potentials are not aware of this mechanism. NNIP simulations are also anticipated to accurately capture the nucleation and propagation of shear loops on {112} planes (See Fig. 11(b)), as observed experimentally in BCC materials [5,9,91]. Furthermore, NNIP effectively models the nucleation of loops through a lasso mechanism, a behavior where GAP and tabGAP induced the formation of multiple loops, as observed in Fig. 11(c) at a depth of 1.45 nm. For NNIP, at the maximum indentation depth, it is evident on the sample's surface that displaced atoms align with the slip planes in a characteristic three-folded rosette pattern typical for BCC materials in the [111] orientation (Fig. 11(d)), formed by [11$\bar{2}$], [$\bar{1}$01], and [0$\bar{1}$1] planes. In contrast, neither GAP nor tabGAP, nor EAM, can adequately incorporate this description due to the lack of information regarding pileup formations. Besides, the nucleation of more loops is noted, but the circumference of the second loop is larger than that of the first loop. The EAM and tabGAP simulations demonstrate a slower and faster process, respectively.

The variations in dislocation and loop nucleations across different potentials originate from two factors: (1) the prediction of the GSFE

+ SIA curve (Fig. 6(c)) varies across different potentials, and (2) the indentation surface energy as a function of depth differs among potentials, as demonstrated in Fig. S9 of the SM.

4. Discussion and conclusions

Interatomic potentials developed before the present work, although adequate for many applications, need to be improved for nanoindentation simulations. For example, J. Byggmästar et al. [63] developed a GAP potential for Mo, demonstrating accuracy and transferability for elastic, thermal, liquid, defect, and surface properties. However, this potential failed to produce reliable data for the shear stress in the elastic region in the early stages of the nanoindentation simulation. Furthermore, in contrast to the NNIP developed here, many prismatic loops were nucleated during the nanoindentation (see Fig. 11), potentially due to insufficient information in the energy landscape regarding the dislocation cores, a fact that was illustrated based on the similarity of the GSF configurations with the dislocation cores as depicted in Fig. 6.

The tabGAP potentials are designed for complex multi-element materials [48], employing simple low-dimensional descriptors. Although tabGAP potentials have notable accuracy for entropy alloys [62], the same issues as the GAP potential arise when it comes to single element BCC Mo. As mentioned earlier, the tabGAP potential leads to nucleation of too many prismatic dislocation loops in the nanoindentation simulations (see Fig. 11). Moreover, accurate predictions of shear stress in the initial phases of the nanoindentation simulations were not achieved.

The EAM/FS potential utilized in the present work [65], originally designed for radiation damage simulations, failed to accurately produce GSFE curve for Mo in both pristine crystalline and GSF configurations representing dislocation cores. Consequently, it is unclear whether or not this potential can reliably predict dislocation nucleation during indentation. In addition, similar to the other potentials, it does not correctly predict the nanoindentation shear stress.

Considering the challenges faced in nanoindentation simulations, the presence of a well-developed methodology to tackle these issues would be highly beneficial. In this work, we met this goal by introducing to the training dataset new configurations which resemble the local atomic environments of an indented sample. The similarity measurements presented here ensure the relevance of the newly introduced structures to a nanoindentation simulation. To the best of our knowledge, this study represents the first attempt to develop a MLFF specifically designed for nanoindentation simulations. The novel configurations introduced here could aid the development of MLFFs for other materials.

CRediT authorship contribution statement

Amirhossein D. Naghdi: Writing – review & editing, Writing – original draft, Visualization, Validation, Methodology, Formal analysis, Data curation, Conceptualization. **Franco Pellegrini:** Writing – review & editing, Methodology, Investigation, Formal analysis, Conceptualization. **Emine Küçükbenli:** Writing – review & editing, Methodology, Investigation, Conceptualization. **Dario Massa:** Writing – review & editing, Methodology, Data curation. **F. Javier Dominguez–Gutierrez:** Writing – review & editing, Visualization, Methodology, Data curation. **Efthimios Kaxiras:** Writing – review & editing, Supervision, Formal analysis, Conceptualization. **Stefanos Papanikolaou:** Writing – review & editing, Supervision, Methodology, Investigation, Formal analysis, Conceptualization.

Declaration of competing interest

The authors declare that they have no known competing financial interests or personal relationships that could have appeared to influence the work reported in this paper.

Acknowledgments

We acknowledge support from the European Union Horizon 2020 Research and Innovation Programme under grant agreement no. 857470 and from the European Regional Development Fund via the Foundation for Polish Science International Research Agenda PLUS program grant No. MAB PLUS/2018/8.

Appendix A. Supplementary data

Supplementary material related to this article can be found online at https://doi.org/10.1016/j.actamat.2024.120200.

References

[1] J.-Y. Kim, J.R. Greer, Tensile and compressive behavior of gold and molybdenum single crystals at the nano-scale, Acta Mater. 57 (17) (2009) 5245–5253, http://dx.doi.org/10.1016/j.actamat.2009.07.027, URL https://www.sciencedirect.com/science/article/pii/S1359645409004510.

[2] J.-Y. Kim, D. Jang, J.R. Greer, Crystallographic orientation and size dependence of tension–compression asymmetry in molybdenum nano-pillars, Int. J. Plast. 28 (1) (2012) 46–52, http://dx.doi.org/10.1016/j.ijplas.2011.05.015, URL https://www.sciencedirect.com/science/article/pii/S0749641911000994.

[3] M. Motamedi, A. Naghdi, S. Jalali, Effect of temperature on properties of aluminum/single-walled carbon nanotube nanocomposite by molecular dynamics simulation, Proc. Inst. Mech. Eng. C 234 (2) (2020) 635–642, http://dx.doi.org/10.1177/0954406219878760.

[4] C.A. Schuh, Nanoindentation studies of materials, Mater. Today 9 (5) (2006) 32–40, http://dx.doi.org/10.1016/S1369-7021(06)71495-X.

[5] J. Varillas, J. Ocenasek, J. Torner, J. Alcala, Unraveling deformation mechanisms around FCC and BCC nanocontacts through slip trace and pileup topography analyses, Acta Mater. 125 (2017) 431–441, http://dx.doi.org/10.1016/j.actamat.2016.11.067.

[6] L. Kurpaska, F. Dominguez-Gutierrez, Y. Zhang, K. Mulewska, H. Bei, W. Weber, A. Kosińska, W. Chrominski, I. Jozwik, R. Alvarez-Donado, S. Papanikolaou, J. Jagielski, M. Alava, Effects of Fe atoms on hardening of a nickel matrix: Nanoindentation experiments and atom-scale numerical modeling, Mater. Des. 217 (2022) 110639, http://dx.doi.org/10.1016/j.matdes.2022.110639, URL https://www.sciencedirect.com/science/article/pii/S026412752200260X.

[7] S. Pathak, S.R. Kalidindi, Spherical nanoindentation stress strain curves, Mater. Sci. Eng. R 91 (2015) 1–36.

[8] G.Z. Voyiadjis, M. Yaghoobi, Review of nanoindentation size effect: Experiments and atomistic simulation, Crystals 7 (10) (2017) 321.

[9] T. Remington, C. Ruestes, E. Bringa, B. Remington, C. Lu, B. Kad, M. Meyers, Plastic deformation in nanoindentation of tantalum: A new mechanism for prismatic loop formation, Acta Mater. 78 (2014) 378–393, http://dx.doi.org/10.1016/j.actamat.2014.06.058, URL https://www.sciencedirect.com/science/article/pii/S1359645414004881.

[10] J. Gagel, D. Weygand, P. Gumbsch, Formation of extended prismatic dislocation structures under indentation, Acta Mater. 111 (2016) 399.

[11] A. Naghdi, F.J. Dominguez-Gutierrez, W.Y. Huo, K. Karimi, S. Papanikolaou, Dynamic nanoindentation and short-range order in equiatomic nicocr medium entropy alloy lead to novel density wave ordering, 2022, arXiv:2211.05436.

[12] M. Taneike, F. Abe, K. Sawada, Creep-strengthening of steel at high temperatures using nano-sized carbonitride dispersions, Nature 424 (6946) (2003) 294–296, http://dx.doi.org/10.1038/nature01740.

[13] M.A. Haque, M.T.A. Saif, In-situ tensile testing of nano-scale specimens in SEM and TEM, Exp. Mech. 42 (1) (2002) 123–128, http://dx.doi.org/10.1007/BF02411059.

[14] J.T.M. De Hosson, W.A. Soer, A.M. Minor, Z. Shan, E.A. Stach, S.A. Syed Asif, O.L. Warren, In situ TEM nanoindentation and dislocation-grain boundary interactions: a tribute to david brandon, J. Mater. Sci. 41 (23) (2006) 7704–7719, http://dx.doi.org/10.1007/s10853-006-0472-2.

[15] K. Durst, B. Backes, M. Göken, Indentation size effect in metallic materials: Correcting for the size of the plastic zone, Scr. Mater. 52 (11) (2005) 1093–1097, http://dx.doi.org/10.1016/j.scriptamat.2005.02.009, URL https://www.sciencedirect.com/science/article/pii/S1359646205000941.

[16] Maier-Kiener, Verena, Durst, Karsten, Advanced nanoindentation testing for studying strain-rate sensitivity and activation volume, JOM 69 (11) (2017) 2246–2255, http://dx.doi.org/10.1007/s11837-017-2536-y.

[17] O. Casals, J. Očenašek, J. Alcala, Crystal plasticity finite element simulations of pyramidal indentation in copper single crystals, Acta Mater. 55 (1) (2007) 55–68, http://dx.doi.org/10.1016/j.actamat.2006.07.018, URL https://www.sciencedirect.com/science/article/pii/S1359645406005295.

[18] R. Smith, D. Christopher, S.D. Kenny, A. Richter, B. Wolf, Defect generation and pileup of atoms during nanoindentation of Fe single crystals, Phys. Rev. B 67 (2003) 245405, http://dx.doi.org/10.1103/PhysRevB.67.245405, URL https://link.aps.org/doi/10.1103/PhysRevB.67.245405.

[19] S. Swaddiwudhipong, K. Tho, J. Hua, Z. Liu, Mechanism-based strain gradient plasticity in C0 axisymmetric element, Int. J. Solids Struct. 43 (5) (2006) 1117–1130, http://dx.doi.org/10.1016/j.ijsolstr.2005.05.026, URL https://www.sciencedirect.com/science/article/pii/S0020768305002921.

[20] F. Dominguez-Gutierrez, S. Papanikolaou, A. Esfandiarpour, P. Sobkowicz, M. Alava, Nanoindentation of single crystalline Mo: Atomistic defect nucleation and thermomechanical stability, Mater. Sci. Eng. A 826 (2021) 141912, http://dx.doi.org/10.1016/j.msea.2021.141912, URL https://www.sciencedirect.com/science/article/pii/S0921509321011783.

[21] D. Kramer, K. Yoder, W. Gerberich, Surface constrained plasticity: Oxide rupture and the yield point process, Phil. Mag. A 81 (2001) 2033–2058, http://dx.doi.org/10.1080/01418610108216651.

[22] M.M. Biener, J. Biener, A.M. Hodge, A.V. Hamza, Dislocation nucleation in BCC Ta single crystals studied by nanoindentation, Phys. Rev. B 76 (2007) 165422, http://dx.doi.org/10.1103/PhysRevB.76.165422, URL https://link.aps.org/doi/10.1103/PhysRevB.76.165422.

[23] G.Z. Voyiadjis, D. Faghihi, Microstructure to macro-scale using gradient plasticity with temperature and rate dependent length scale, Procedia IUTAM 3 (2012) 205–227, http://dx.doi.org/10.1016/j.piutam.2012.03.014, IUTAM Symposium on Linking Scales in Computations: From Microstructure to Macro-scale Properties, URL https://www.sciencedirect.com/science/article/pii/S2210983812000156.

[24] K.P.E. Plummer, The Temperature Dependence of Plasticity in Molybdenum (Ph.D. thesis), University of Oxford, 2019.

[25] K. Frydrych, F. Dominguez-Gutierrez, M. Alava, S. Papanikolaou, Multiscale nanoindentation modelling of concentrated solid solutions: A continuum plasticity model, Mech. Mater. 181 (2023) 104644, http://dx.doi.org/10.1016/j.mechmat.2023.104644, URL https://www.sciencedirect.com/science/article/pii/S016766362300090X.

[26] J.A. Knapp, D.M. Follstaedt, S.M. Myers, J.C. Barbour, T.A. Friedmann, Finite-element modeling of nanoindentation, J. Appl. Phys. 85 (3) (1999) 1460–1474, http://dx.doi.org/10.1063/1.369178, arXiv:https://pubs.aip.org/aip/jap/article-pdf/85/3/1460/10597542/1460_1_online.pdf.

[27] M. Lichinchi, C. Lenardi, J. Haupt, R. Vitali, Simulation of berkovich nanoindentation experiments on thin films using finite element method, Thin Solid Films 312 (1) (1998) 240–248, http://dx.doi.org/10.1016/S0040-6090(97)00739-6, URL https://www.sciencedirect.com/science/article/pii/S0040609097007396.

[28] C. Zhou, S.B. Biner, R. LeSar, Discrete dislocation dynamics simulations of plasticity at small scales, Acta Mater. 58 (5) (2010) 1565–1577, http://dx.doi.org/10.1016/j.actamat.2009.11.001, URL https://www.sciencedirect.com/science/article/pii/S1359645409007678.

[29] C. Motz, D. Weygand, J. Senger, P. Gumbsch, Micro-bending tests: A comparison between three-dimensional discrete dislocation dynamics simulations and experiments, Acta Mater. 56 (9) (2008) 1942–1955, http://dx.doi.org/10.1016/j.actamat.2007.12.053, URL https://www.sciencedirect.com/science/article/pii/S1359645408000062.

[30] H. Song, H. Yavas, E.V. der Giessen, S. Papanikolaou, Discrete dislocation dynamics simulations of nanoindentation with pre-stress: Hardness and statistics of abrupt plastic events, J. Mech. Phys. Solids 123 (2019) 332–347, http://dx.doi.org/10.1016/j.jmps.2018.09.005, The N.A. Fleck 60th Anniversary Volume, URL https://www.sciencedirect.com/science/article/pii/S0022509618305027.

[31] G. Po, M.S. Mohamed, T. Crosby, C. Erel, A. El-Azab, N. Ghoniem, Recent progress in discrete dislocation dynamics and its applications to micro plasticity, JOM 66 (10) (2014) 2108–2120, http://dx.doi.org/10.1007/s11837-014-1153-2.

[32] R. Santos-Güemes, G. Esteban-Manzanares, I. Papadimitriou, J. Segurado, L. Capolungo, J. LLorca, Discrete dislocation dynamics simulations of dislocation-θ' precipitate interaction in Al-Cu alloys, J. Mech. Phys. Solids 118 (2018) 228–244, http://dx.doi.org/10.1016/j.jmps.2018.05.015, URL https://www.sciencedirect.com/science/article/pii/S0022509617310037.

[33] Q. Xu, A. Zaborowska, K. Mulewska, W. Huo, K. Karimi, F.J. Domínguez-Gutiérrez, Ł. Kurpaska, M.J. Alava, S. Papanikolaou, Atomistic insights into nanoindentation-induced deformation of alpha-Al2O3 single crystals, Vacuum 219 (2024) 112733, http://dx.doi.org/10.1016/j.vacuum.2023.112733, URL https://www.sciencedirect.com/science/article/pii/S0042207X23009302.

[34] F.J. Domínguez-Gutiérrez, P. Grigorev, A. Naghdi, J. Byggmästar, G.Y. Wei, T.D. Swinburne, S. Papanikolaou, M.J. Alava, Nanoindentation of tungsten: From interatomic potentials to dislocation plasticity mechanisms, Phys. Rev. Mater. 7 (2023) 043603, http://dx.doi.org/10.1103/PhysRevMaterials.7.043603, URL https://link.aps.org/doi/10.1103/PhysRevMaterials.7.043603.

[35] A.H. Naghdi, K. Karimi, A.E. Poisvert, A. Esfandiarpour, R. Alvarez, P. Sobkowicz, M. Alava, S. Papanikolaou, Dislocation plasticity in equiatomic NiCoCr alloys: Effect of short-range order, Phys. Rev. B 107 (2023) 094109, http://dx.doi.org/10.1103/PhysRevB.107.094109, URL https://link.aps.org/doi/10.1103/PhysRevB.107.094109.

[36] K. Karimi, A. Esfandiarpour, S. Papanikolaou, Serrated plastic flow in slowly-deforming complex concentrated alloys: universal signatures of dislocation avalanches, 2023, arXiv:2310.03828.

[37] K. Karimi, S. Papanikolaou, Tuning brittleness in multi-component metallic glasses through chemical disorder aging, 2023, arXiv:2309.11867.

[38] J. Behler, M. Parrinello, Generalized neural-network representation of high-dimensional potential-energy surfaces, Phys. Rev. Lett. 98 (2007) 146401, http://dx.doi.org/10.1103/PhysRevLett.98.146401, URL https://link.aps.org/doi/10.1103/PhysRevLett.98.146401.

[39] A.P. Bartók, M.C. Payne, R. Kondor, G. Csányi, Gaussian approximation potentials: The accuracy of quantum mechanics, without the electrons, Phys. Rev. Lett. 104 (2010) 136403, http://dx.doi.org/10.1103/PhysRevLett.104.136403, URL https://link.aps.org/doi/10.1103/PhysRevLett.104.136403.

[40] A. Thompson, L. Swiler, C. Trott, S. Foiles, G. Tucker, Spectral neighbor analysis method for automated generation of quantum-accurate interatomic potentials, J. Comput. Phys. 285 (2015) 316–330, http://dx.doi.org/10.1016/j.jcp.2014.12.018, URL https://www.sciencedirect.com/science/article/pii/S0021999114008353.

[41] A.V. Shapeev, Moment tensor potentials: A class of systematically improvable interatomic potentials, Multiscale Model. Simul. 14 (3) (2016) 1153–1173, http://dx.doi.org/10.1137/15M1054183.

[42] A. Glielmo, C. Zeni, A. De Vita, Efficient nonparametric n-body force fields from machine learning, Phys. Rev. B 97 (2018) 184307, http://dx.doi.org/10.1103/PhysRevB.97.184307, URL https://link.aps.org/doi/10.1103/PhysRevB.97.184307.

[43] L. Zhang, J. Han, H. Wang, R. Car, W. E, Deep potential molecular dynamics: A scalable model with the accuracy of quantum mechanics, Phys. Rev. Lett. 120 (2018) 143001, http://dx.doi.org/10.1103/PhysRevLett.120.143001, URL https://link.aps.org/doi/10.1103/PhysRevLett.120.143001.

[44] J. Behler, Perspective: Machine learning potentials for atomistic simulations, J. Chem. Phys. 145 (17) (2016) 170901, http://dx.doi.org/10.1063/1.4966192.

[45] Y. Shaidu, E. Küçükbenli, R. Lot, F. Pellegrini, E. Kaxiras, S. de Gironcoli, A systematic approach to generating accurate neural network potentials: the case of carbon, npj Comput. Mater. 7 (1) (2021) 52, http://dx.doi.org/10.1038/s41524-021-00508-6.

[46] Q.-J. Li, E. Küçükbenli, S. Lam, B. Khaykovich, E. Kaxiras, J. Li, Development of robust neural-network interatomic potential for molten salt, Cell Rep. Phys. Sci. 2 (3) (2021) 100359, http://dx.doi.org/10.1016/j.xcrp.2021.100359, URL https://www.sciencedirect.com/science/article/pii/S2666386421000448.

[47] Y. Shiihara, R. Kanazawa, D. Matsunaka, I. Lobzenko, T. Tsuru, M. Kohyama, H. Mori, Artificial neural network molecular mechanics of iron grain boundaries, Scr. Mater. 207 (2022) 114268, http://dx.doi.org/10.1016/j.scriptamat.2021.114268, URL https://www.sciencedirect.com/science/article/pii/S1359646221005480.

[48] J. Byggmästar, K. Nordlund, F. Djurabekova, Simple machine-learned interatomic potentials for complex alloys, Phys. Rev. Mater. 6 (2022) 083801, http://dx.doi.org/10.1103/PhysRevMaterials.6.083801, URL https://link.aps.org/doi/10.1103/PhysRevMaterials.6.083801.

[49] J. Vandermause, S.B. Torrisi, S. Batzner, Y. Xie, L. Sun, A.M. Kolpak, B. Kozinsky, On-the-fly active learning of interpretable Bayesian force fields for atomistic rare events, npj Comput. Mater. 6 (1) (2020) 20, http://dx.doi.org/10.1038/s41524-020-0283-z.

[50] E.V. Podryabinkin, A.V. Shapeev, Active learning of linearly parametrized interatomic potentials, Comput. Mater. Sci. 140 (2017) 171–180, http://dx.doi.org/10.1016/j.commatsci.2017.08.031, URL https://www.sciencedirect.com/science/article/pii/S0927025617304536.

[51] F. Pellegrini, R. Lot, Y. Shaidu, E. Küçükbenli, PANNA 2.0: Efficient neural network interatomic potentials and new architectures, 2023, arXiv:2305.11805.

[52] A. Musaelian, S. Batzner, A. Johansson, L. Sun, C.J. Owen, M. Kornbluth, B. Kozinsky, Learning local equivariant representations for large-scale atomistic dynamics, Nature Commun. 14 (1) (2023) 579, http://dx.doi.org/10.1038/s41467-023-36329-y.

[53] I. Batatia, S. Batzner, D.P. Kovács, A. Musaelian, G.N.C. Simm, R. Drautz, C. Ortner, B. Kozinsky, G. Csányi, The design space of e(3)-equivariant atom-centered interatomic potentials, (arXiv:2205.06643) 2022, http://dx.doi.org/10.48550/arXiv.2205.06643, arXiv:2205.06643.

[54] C. Zeni, A. Anelli, A. Glielmo, K. Rossi, Exploring the robust extrapolation of high-dimensional machine learning potentials, Phys. Rev. B 105 (2022) 165141, http://dx.doi.org/10.1103/PhysRevB.105.165141, URL https://link.aps.org/doi/10.1103/PhysRevB.105.165141.

[55] I. Batatia, D.P. Kovacs, G. Simm, C. Ortner, G. Csanyi, MACE: Higher order equivariant message passing neural networks for fast and accurate force fields, in: S. Koyejo, S. Mohamed, A. Agarwal, D. Belgrave, K. Cho, A. Oh (Eds.), in: Advances in Neural Information Processing Systems, vol. 35, Curran Associates, Inc., 2022, pp. 11423–11436, URL https://proceedings.neurips.cc/paper_files/paper/2022/file/4a36c3c51af11ed9f34615b81edb5bbc-Paper-Conference.pdf.

[56] T. Miyagawa, K. Mori, N. Kato, A. Yonezu, Development of neural network potential for MD simulation and its application to TiN, Comput. Mater. Sci. 206 (2022) 111303, http://dx.doi.org/10.1016/j.commatsci.2022.111303, URL https://www.sciencedirect.com/science/article/pii/S0927025622000970.

[57] C.J. Owen, Y. Xie, A. Johansson, L. Sun, B. Kozinsky, Stability, mechanisms and kinetics of emergence of au surface reconstructions using Bayesian force fields, 2023, arXiv:2308.07311.

[58] C.J. Owen, N. Marcella, Y. Xie, J. Vandermause, A.I. Frenkel, R.G. Nuzzo, B. Kozinsky, Unraveling the catalytic effect of hydrogen adsorption on pt nanoparticle shape-change, 2023, arXiv:2306.00901.

[59] A.M. Goryaeva, J. Dérès, C. Lapointe, P. Grigorev, T.D. Swinburne, J.R. Kermode, L. Ventelon, J. Baima, M.-C. Marinica, Efficient and transferable machine learning potentials for the simulation of crystal defects in BCC Fe and W, Phys. Rev. Mater. 5 (2021) 103803, http://dx.doi.org/10.1103/PhysRevMaterials.5.103803, URL https://link.aps.org/doi/10.1103/PhysRevMaterials.5.103803.

[60] J. Byggmästar, A. Hamedani, K. Nordlund, F. Djurabekova, Machine-learning interatomic potential for radiation damage and defects in tungsten, Phys. Rev. B 100 (2019) 144105, http://dx.doi.org/10.1103/PhysRevB.100.144105, URL https://link.aps.org/doi/10.1103/PhysRevB.100.144105.

[61] G. Nikoulis, J. Byggmästar, J. Kioseoglou, K. Nordlund, F. Djurabekova, Machine-learning interatomic potential for W–Mo alloys, J. Phys.: Condens. Matter. 33 (31) (2021) 315403, http://dx.doi.org/10.1088/1361-648X/ac03d1.

[62] J. Byggmästar, K. Nordlund, F. Djurabekova, Modeling refractory high-entropy alloys with efficient machine-learned interatomic potentials: Defects and segregation, Phys. Rev. B 104 (2021) 104101, http://dx.doi.org/10.1103/PhysRevB.104.104101, URL https://link.aps.org/doi/10.1103/PhysRevB.104.104101.

[63] J. Byggmästar, K. Nordlund, F. Djurabekova, Gaussian approximation potentials for body-centered-cubic transition metals, Phys. Rev. Mater. 4 (2020) 093802, http://dx.doi.org/10.1103/PhysRevMaterials.4.093802, URL https://link.aps.org/doi/10.1103/PhysRevMaterials.4.093802.

[64] R. Lot, F. Pellegrini, Y. Shaidu, E. Küçükbenli, PANNA: Properties from artificial neural network architectures, Comput. Phys. Comm. 256 (2020) 107402, http://dx.doi.org/10.1016/j.cpc.2020.107402, URL https://www.sciencedirect.com/science/article/pii/S0010465520301843.

[65] E. Salonen, T. Järvi, K. Nordlund, J. Keinonen, Effects of the surface structure and cluster bombardment on the self-sputtering of molybdenum, J. Phys.: Condens. Matter. 15 (34) (2003) 5845, http://dx.doi.org/10.1088/0953-8984/15/34/314.

[66] Z. Li, J.R. Kermode, A. De Vita, Molecular dynamics with on-the-fly machine learning of quantum-mechanical forces, Phys. Rev. Lett. 114 (2015) 096405, http://dx.doi.org/10.1103/PhysRevLett.114.096405, URL https://link.aps.org/doi/10.1103/PhysRevLett.114.096405.

[67] A.P. Bartók, R. Kondor, G. Csányi, On representing chemical environments, Phys. Rev. B 87 (2013) 184115, http://dx.doi.org/10.1103/PhysRevB.87.184115, URL https://link.aps.org/doi/10.1103/PhysRevB.87.184115.

[68] M. Abadi, et al., TensorFlow: Large-scale machine learning on heterogeneous systems, 2015, Software available from tensorflow.org, URL https://www.tensorflow.org/.

[69] J.S. Smith, O. Isayev, A.E. Roitberg, ANI-1: an extensible neural network potential with DFT accuracy at force field computational cost, Chem. Sci. 8 (2017) 3192–3203, http://dx.doi.org/10.1039/C6SC05720A.

[70] J. Byggmästar, K. Nordlund, F. Djurabekova, Gaussian approximation potentials for body-centered-cubic transition metals, Phys. Rev. Mater. 4 (2020) 093802, http://dx.doi.org/10.1103/PhysRevMaterials.4.093802, URL https://link.aps.org/doi/10.1103/PhysRevMaterials.4.093802.

[71] P. Giannozzi, et al., QUANTUM ESPRESSO: a modular and open-source software project for quantum simulations of materials, J. Phys.: Condens. Matter. 21 (39) (2009) 395502, http://dx.doi.org/10.1088/0953-8984/21/39/395502.

[72] P. Giannozzi, et al., Advanced capabilities for materials modelling with Quantum ESPRESSO, J. Phys.: Condens. Matter. 29 (46) (2017) 465901, http://dx.doi.org/10.1088/1361-648x/aa8f79.

[73] G. Prandini, A. Marrazzo, I.E. Castelli, N. Mounet, N. Marzari, Precision and efficiency in solid-state pseudopotential calculations, npj Comput. Mater. 4 (1) (2018) 72, http://dx.doi.org/10.1038/s41524-018-0127-2.

[74] K. Lejaeghere, et al., Reproducibility in density functional theory calculations of solids, Science 351 (6280) (2016) aad3000, http://dx.doi.org/10.1126/science.aad3000, arXiv:https://www.science.org/doi/pdf/10.1126/science.aad3000, URL https://www.science.org/doi/abs/10.1126/science.aad3000.

[75] D.R. Hamann, Optimized norm-conserving Vanderbilt pseudopotentials, Phys. Rev. B 88 (2013) 085117, http://dx.doi.org/10.1103/PhysRevB.88.085117, URL https://link.aps.org/doi/10.1103/PhysRevB.88.085117.

[76] H.J. Monkhorst, J.D. Pack, Special points for Brillouin-zone integrations, Phys. Rev. B 13 (1976) 5188–5192, http://dx.doi.org/10.1103/PhysRevB.13.5188, URL https://link.aps.org/doi/10.1103/PhysRevB.13.5188.

[77] M. Methfessel, A.T. Paxton, High-precision sampling for Brillouin-zone integration in metals, Phys. Rev. B 40 (1989) 3616–3621, http://dx.doi.org/10.1103/PhysRevB.40.3616, URL https://link.aps.org/doi/10.1103/PhysRevB.40.3616.

[78] D. Chung, W. Buessem, The voigt-reuss-hill approximation and elastic moduli of polycrystalline MgO, CaF2, β-ZnS, ZnSe, and CdTe, J. Appl. Phys. 38 (6) (1967) 2535–2540.

[79] THERMO_PW driver for QE (Github link). URL https://dalcorso.github.io/thermo_pw/.

[80] D.P. Kingma, J. Ba, Adam: A method for stochastic optimization, 2017, arXiv:1412.6980.

[81] E. Nunez, K. Bashandeh, A. Polycarpou, Thermal and mechanical properties of polymer coatings, 2020, pp. 157–175, http://dx.doi.org/10.1201/9780429199226-9.

[82] W.C. Oliver, G.M. Pharr, An improved technique for determining hardness and elastic modulus using load and displacement sensing indentation experiments, J. Mater. Res. 7 (1992) 1564–1583, http://dx.doi.org/10.1557/JMR.1992.1564.

[83] J.J. Möller, E. Bitzek, BDA: A novel method for identifying defects in body-centered cubic crystals, MethodsX 3 (2016) 279–288, http://dx.doi.org/10.1016/j.mex.2016.03.013.

[84] A. Stukowski, Visualization and analysis of atomistic simulation data with OVITO-the Open Visualization Tool, Modelling Simul. Mater. Sci. Eng. 18 (1) (2010) http://dx.doi.org/10.1088/0965-0393/18/1/015012.

[85] A. Stukowski, Computational analysis methods in atomistic modeling of crystals, JOM 66 (3) (2014) 399–407, http://dx.doi.org/10.1007/s11837-013-0827-5.

[86] J. Rumble, CRC Handbook of Chemistry and Physics, hundredth ed., CRC Press, Boca Raton, FL, 2019.

[87] S. Zhang, D. Legut, R. Zhang, PNADIS: An automated Peierls–Nabarro analyzer for dislocation core structure and slip resistance, Comput. Phys. Comm. 240 (2019) 60–73.

[88] R. Peierls, The size of a dislocation, Proc. Phys. Soc. 52 (1) (1940) 34–37.

[89] F. Nabarro, Dislocations in a simple cubic lattice, Proc. Phys. Soc. 59 (2) (1947) 256.

[90] S. Jakob, A. Leitner, A. Lorich, M. Eidenberger-Schober, W. Knabl, R. Pippan, H. Clemens, V. Maier-Kiener, Influence of crystal orientation and Berkovich tip rotation on the mechanical characterization of grain boundaries in molybdenum, Mater. Des. 182 (2019) 107998, http://dx.doi.org/10.1016/j.matdes.2019.107998, URL https://www.sciencedirect.com/science/article/pii/S0264127519304368.

[91] K. Mulewska, F. Dominguez-Gutierrez, D. Kalita, J. Byggmästar, G. Wei, W. Chromiński, S. Papanikolaou, M. Alava, Ł. Kurpaska, J. Jagielski, Selfâ€“ion irradiation of high purity iron: Unveiling plasticity mechanisms through nanoindentation experiments and large-scale atomistic simulations, J. Nucl. Mater. 586 (2023) 154690, http://dx.doi.org/10.1016/j.jnucmat.2023.154690, URL https://www.sciencedirect.com/science/article/pii/S0022311523004580.